Article:

Silva, SCD, de Souza, EA, Pessu, F orcid.org/0000-0003-3587-4309 et al. (4 more authors) (2019) Cracking mechanism in API 5L X65 steel in a CO-₂saturated environment. Engineering Failure Analysis, 99. pp. 273-291. ISSN 1350-6307

https://doi.org/10.1016/j.engfailanal.2019.02.031

Cracking mechanism in API 5L X65 steel in a CO_2-saturated environment

Samara Cruz da Silva[1]*, Eduardo Alencar de Souza[1], Frederick Oritseweneye Pessu[2], Yong Hua[2], Richard James Barker[2], Anne Neville[2], José Antônio da Cunha Ponciano Gomes[1]

[1]Federal University of Rio de Janeiro, Department of Metallurgical and Materials Engineering, Labcorr, Rio de Janeiro, Brazil

[2]Institute of Functional Surfaces, Faculty of Mechanical Engineering, University of Leeds, Leeds, United Kingdom

ABSTRACT

Hydrogen charging in low alloy steels poses a significant problem in the oil and gas industry in mixed carbon dioxide (CO_2) and hydrogen sulphide (H_2S) containing environments. The risk of Sulphide Stress Cracking (SSC) is usually related to the propensity for hydrogen permeation to occur, which is typically determined based on the solution pH and H_2S partial pressure. Detrimental hydrogen effects are not commonly expected in CO_2 aqueous environments. However, the acid nature of these environments and the high corrosion rates expected justify the assessment of cracking susceptibility of carbon steel in a CO_2-saturated environment as presented in this work. The focus of this investigation is to understand how different surface films/corrosion products influence the hydrogen permeation and cracking mechanism of an API 5L X65 carbon steel in a saturated CO_2 environment. The experiments were carried out to assess hydrogen permeation at open circuit potential on steel samples which were either wet-ground, or pre-filmed with iron carbide (Fe_3C) rich or iron carbonate ($FeCO_3$) layers. Tafel measurements were also performed to determine the effect of the surface composition on the cathodic reactions. Slow strain rate tests (SSRT) were conducted in order to evaluate the effects of hydrogen on the cracking mechanisms of the steel in this sweet environment. Results indicated that at open circuit conditions, Fe_3C was able to increase the steady state hydrogen permeation current due to accentuation of the cathodic hydrogen-evolution reaction. Although $FeCO_3$ suppressed the cathodic reaction at the steel surface, the development of the protective and densely packed

---

* Corresponding Author – E-mail address: maraufrj@hotmail.com

crystalline layer increased hydrogen uptake marginally from that of the ground steel reduced. SSRT indicated a very moderate loss of ductility in wet-ground and $FeCO_3$ steel surface conditions. However, a more significant reduction in area was observed in the tests carried out on Fe_3C rich samples. These results imply that a corroded API 5L X65 steel surface in a CO_2 rich environment can enhance the hydrogen embrittlement (HE) susceptibility and as such, hydrogen permeation susceptibility needs to be considered in material selection.

Keywords: hydrogen embrittlement, surface layers, corrosion, pipeline failures.

1. INTRODUCTION

Carbon steel pipelines play an extremely important role throughout the world as a transporting system of oil and gas over long distances from their sources to ultimate consumers. Under specific operating conditions, the risk of hydrogen embrittlement of steels can be one of the primary concerns. The presence of hydrogen sulphide (H_2S) in combination with carbon dioxide (CO_2) has been shown to enhance the hydrogen charging of carbon steel and increase hydrogen embrittlement susceptibility [1].

In the combined presence of H_2S and CO_2, sulphide stress corrosion cracking (SSC) is one of the main failure modes of carbon steel pipelines. The flux of hydrogen through steel is the main driving force for SSC and this is believed to be predominantly dependent upon the solution pH and partial pressure of H_2S (pH_2S) [2,3]. However, within different oil and gas environments, it is possible for different surface films to evolve on the steel surface. Some of these film layers have been shown to promote corrosion of the steel surface through galvanic effects or internal acidification, as is the case with iron carbide (Fe_3C) [4,5] while other films are capable of stifling the corrosion reaction, such as iron carbonate ($FeCO_3$) [6-8]. Given that such film formation processes have a strong impact on corrosion and the cathodic reaction rates, the film formation process may have a direct influence on the hydrogen charging mechanism. The presence of different films may potentially modify the net charging flux.

The purpose of this work is to investigate the influence of corrosion product layer on the hydrogen charging and permeation characteristics of API 5L X65 carbon steel in a purely CO_2-containing environment. This objective is achieved through the comparison of wet-ground steel samples compared to those with Fe_3C and $FeCO_3$ rich surfaces. The tested samples are filmed under controlled conditions adjusted to produce consistent and repeatable Fe_3C and $FeCO_3$ layers on the steel surface. Cathodic Tafel measurements are then performed in CO_2-saturated 3.5 wt.% NaCl solution, pH 3.8, room temperature to assess the effect of the film on the cathodic reaction. In the same solution, hydrogen permeation measurements are performed using 3mm thick steel samples under the same conditions to determine the influence of the film on the hydrogen permeation rates. Slow Strain Rate Tests (SSRT) were performed in order to investigate the effect of hydrogen on tensile samples of carbon steel, according to NACE TM0198 and ASTM G129 [9,10]. These tests were carried out in air - considered as a baseline condition - and in solution using the hydrogen permeation data as a reference to adjust the loading procedure of the different tensile samples.

2. EXPERIMENTAL PROCEDURE

The material used in this study is an API 5L X65 carbon steel. The steel is composed by a ferritic-pearlitic microstructure, as observed from the optical microscope image shown in Figure 1. The image was obtained by polishing the surface using 3 µm diamond suspension to attain a mirror finish, followed by etching in a 2% Nital solution for 10 to 20 seconds. The chemical composition of the steel is also indicated in Table 1.

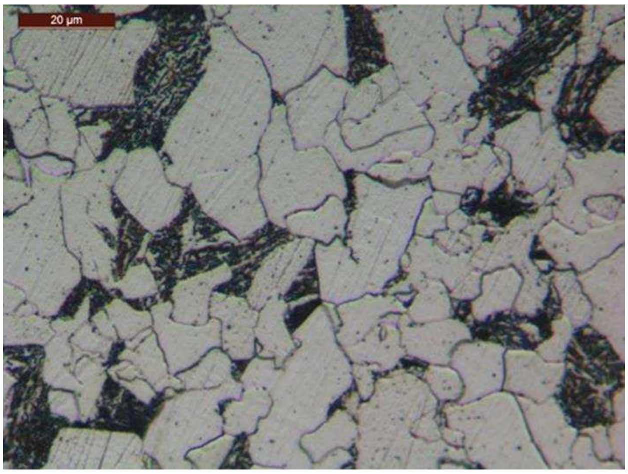

Figure 1: Microstructure ferritic-pearlitic of API 5L X65 steel

Table 1: Elemental composition (wt.%) of API 5L X65 carbon steel

C	Si	Mn	P	S	Cr	Mo	Cu	V	Fe
0.10	0.19	1.43	0.007	0.001	0.12	0.16	0.07	0.09	Balance

The study was divided into three stages; film generation/growth, hydrogen permeation experiments and slow strain rate tests. The details of each stage are outlined in the following sections. In the film formation and hydrogen permeation experiments, samples of 25 mm diameter and 3 mm thickness were used. In SSRT, standards samples of 25.4 mm length and 3.81 mm diameter were used, according to NACE TM0198 [9].

2.1 Film growth/generation experiments

All hydrogen permeation samples were polished on both sides with silicon carbide (SiC) paper grit 1200, both for the film formation tests and for the hydrogen permeation tests. SSRT samples were prepared of the same way.

The first test step was the production of steel samples with different surface compositions. Three surface conditions were accounted to subsequently perform the hydrogen permeation and SSRT. These were:

I. The as-received circular plate sample, was polished on both sides wet-ground for permeation tests, as well as the as-received tensile standard sample for SSRT.

II. The sample with an Fe_3C rich surface generated in a CO_2-saturated 3.5 wt.% NaCl solution at pH 3.8, at 30℃ for 20 hours was placed at the hydrogen charging side of the permeation cell. At the anodic side the wet-ground sample surface was placed; and for SSRT sample, the surface was totally enriched with Fe_3C, at the same condition used for hydrogen permeation samples.

III. The sample with an $FeCO_3$ film generated in a CO_2-saturated 3.5 wt.% NaCl solution at pH 6.6, at 70℃ for 20 hours placed at the hydrogen charging side of the permeation cell. At the anodic side the sample surface was wet-ground was placed; and $FeCO_3$ film surface was formed on SSRT samples at the same condition used for hydrogen permeation samples.

To generate the Fe_3C and $FeCO_3$ surfaces on the permeation and tensile steel samples, specimens were immersed in a 1L CO_2-saturated brine solution, with one side masked off for permeation experiments, at the conditions previously specified. These experiments were performed using the setup shown in Figure 2. The solution was pre-saturated by bubbling in CO_2 for 1 hour and to remove oxygen (O_2) from the system. CO_2 was also bubbled during the experiment to maintain saturation. All film formation experiments were conducted in static conditions with a low stir rate of 250 rpm to provided agitation of the test solution.

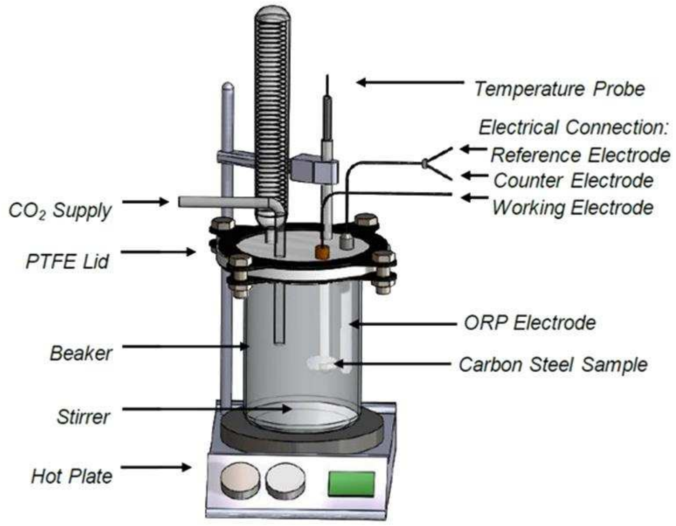

Figure 2: Schematic of test cell for electrochemical measurements during Fe_3C and $FeCO_3$ film formation.

The Linear Polarisation Resistance (LPR) technique was used during the film formation process in order to monitor the correlation between film formation and the corrosion rate. The working electrode was used together with a Ag/AgCl reference electrode and platinum counter electrode to carry out the electrochemical measurements. LPR was determined by polarising the working electrode from -20 mV to +20 mV vs OCP at a scan rate equal to 0.25 mV/s every 15 minutes. The resulting polarisation resistance (R_p) was adjusted based on the solution resistance (determined from AC impedance measurements) to extract the charge transfer resistance (R_{ct}). This resistance was subsequently converted into corrosion rate through the application of the Stern-Geary relationship, using appropriate values of anodic and cathodic Tafel constants determined experimentally and Faraday’s Law.

Once the film formation process was completed at either 30°C/pH 3.8 or 70°C/pH 6.6, the sample was either removed from the test solution, unmasked, cleaned and positioned directly into a Devanathan-Stachurski permeation cell for tests conducted at ambient conditions (CO_2-saturated 3.5 wt.% NaCl brine at pH 3.8) or into the SSRT cell under the same conditions. Samples embedded in resin were placed into a second cell (as shown in Figure 2) for cathodic Tafel polarisation carried out to determine the surface film influence on the cathodic reactions. The cathodic Tafel measurements were performed by polarising from OCP down to -600 mV vs OCP and scan rate equal to 0.25 mV/s. The plots were then corrected for the solution resistance determined using AC impedance measurements to provide accurate relationships between the applied voltages and the measured current.

Separate anodic and cathodic polarisation scans were also performed at the end of each film formation step to determine the appropriate values of anodic and cathodic Tafel constants to support the conversion of the charge-transfer resistance into corrosion rate based on Stern-Geary coefficient in conjunction with Faraday's Law. However, once these anodic and cathodic Tafel measurements were performed, the experiments were ended and no further electrochemical measurements or surface analysis was performed on the system as such extensive polarisation may have changed the characteristics of the surface or contaminated the test solution.

Corrosion current density, i_{corr}, is related to R_p by the Stern-Geary coefficient, as indicated on equation 1.

$$i_{corr} = 10^6(B/R_p) \qquad \text{Eq.1}$$

In which: B is Stern-Geary coefficient; i_{corr} in $\mu A/cm^2$ and B in V/década.

The determination of the linear polarisation resistance (R_p) of the electrode, through equation 2:

$$R_p = \Delta E/\Delta i \qquad \text{Eq. 2}$$

In which: R_p is the linear polarisation resistance in $\Omega.cm^2$; ΔE is the potential variation around the corrosion potential and i is the current density read for each potential scan.

The Stern-Geary coefficient is related to the coefficients of the anodic and cathodic branches of the Tafel curve, being given by the equation 3:

$$B = (\beta_a . \beta_c)/2.3(\beta_a+\beta_c) \qquad \text{Eq. 3}$$

In which: βa is the Tafel coefficient for anodic polarisation and βc is the Tafel coefficient for cathodic polarisation.

Faraday's law is then used to determine corrosion rate using the equation 4:

$$\Delta m = (MA/nF)Q \qquad \text{Eq. 4}$$

In which: Δm represents the mass gain (mg), A is the area (cm^2), M is the molar mass of the formed compound (g/mol), n is the number of electrons involved in the redox process, F is Faraday's constant (C/mol) and Q is the charge corresponding to each cathode peak (mC/cm^2).

2.2 Hydrogen Permeation Experiments

Permeation measurements were performed using a Devanathan-Stachurski cell (Figure 3) at ambient temperature in a CO_2-saturated 3.5 wt.% NaCl brine at pH 3.8. Measurements were conducted on 25 mm diameter, 3 mm thick samples with an exposed surface area of 1 cm^2 to each side of the cell. All tests were performed at OCP.

The left compartment shown in Figure 3 is the cathodic side, in which the generation of hydrogen occurs; in this study the generation of hydrogen was provided by the natural rate of the cathodic reduction of hydrogen ions at OCP. The right compartment of the cell is the anodic side, where the oxidation of atomic hydrogen that diffuses through the steel sample occurs. The anodic side of the cell contained an Ag/AgCl reference electrode (RE), a platinum counter electrode (CE) and the steel sample as the working electrode (WE) for both sides of the cell. The steel sample is located in the central part of the cell and separates the anodic and cathodic compartments.

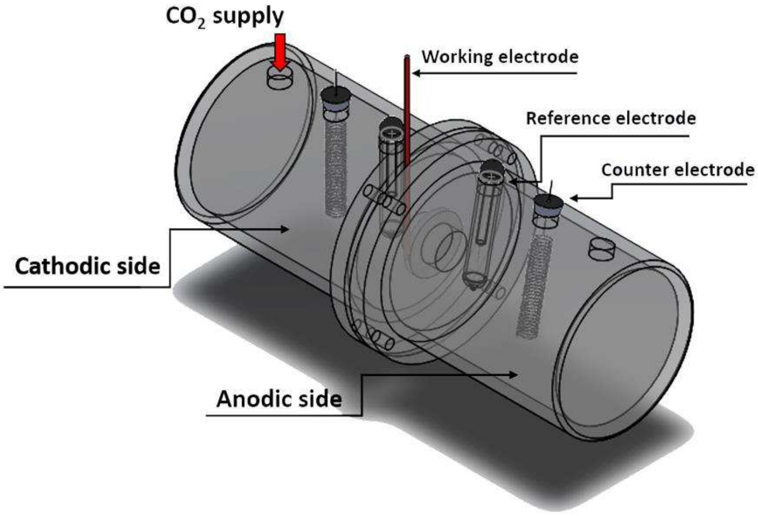

Figure 3: Schematic drawing of Devanathan-Stachurski cell for hydrogen permeation tests. Cathodic side to the left filled with CO_2-saturated 3.5 wt.% NaCl solution. Anodic side to the right filled with 1M NaOH.

For the hydrogen permeation tests, the anodic side was first filled with 1 M NaOH. The OCP was monitored for 2 h, after which a potential of 100 mV vs OCP was applied overnight. After this time, the anodic current had stabilised and the CO_2-saturated 3.5

wt.% NaCl solution was added to the cathodic side and the anodic side current was continuously measured for more 20 h. The test matrix implemented comprised of varying the surface state of the sample at the cathodic side (either wet-ground, Fe_3C rich or $FeCO_3$ rich).

In addition, longer permeation tests were performed to achieve a better understanding of correlation between hydrogen permeation flux and Fe_3C enrichment at the carbon steel surface. This test was performed over 180 h to observe the evolution of the hydrogen permeation current from the first 20 h of test that should be similar to the permeation current corresponding to the wet-ground surface condition, to the elapsed time necessary to produce the Fe_3C enriched surface, when the expected hydrogen permeation current should be higher.

2.3 Slow Strain Rate Tests (SSRT)

Slow Strain Rate Tests were performed in order to investigate the effect of the CO_2 environment on API 5L X65 steel. Tests in air were previously performed aiming to provide a baseline for the assessment of the mechanical response of the steel without any influence of the environment. These results were compared to those obtained in a CO_2-saturated environment for the steel with different surface conditions. Standard samples were used, according to NACE TM0198. All tests were performed at OCP. Figure 4 shows a schematic drawing of cell used for SSRT.

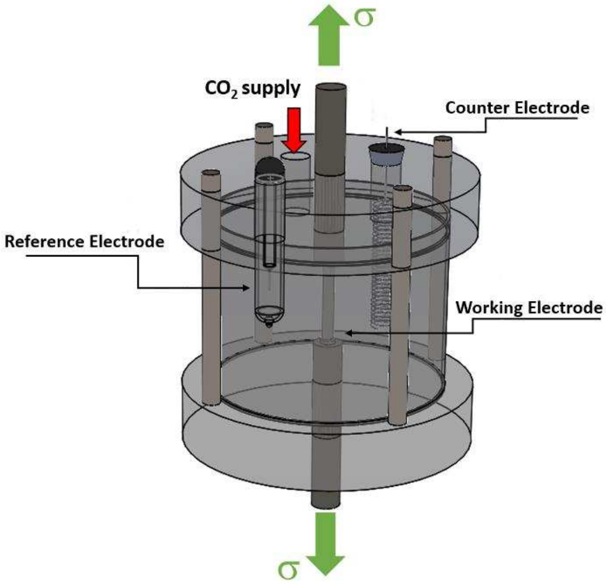

Figure 4: Schematic drawing of cell used in the slow strain rate tests

SSRT conditions were defined according to the flow sheet and schematic drawing of the hydrogen permeation curve presented in Figure 5 and in Figure 6, respectively.

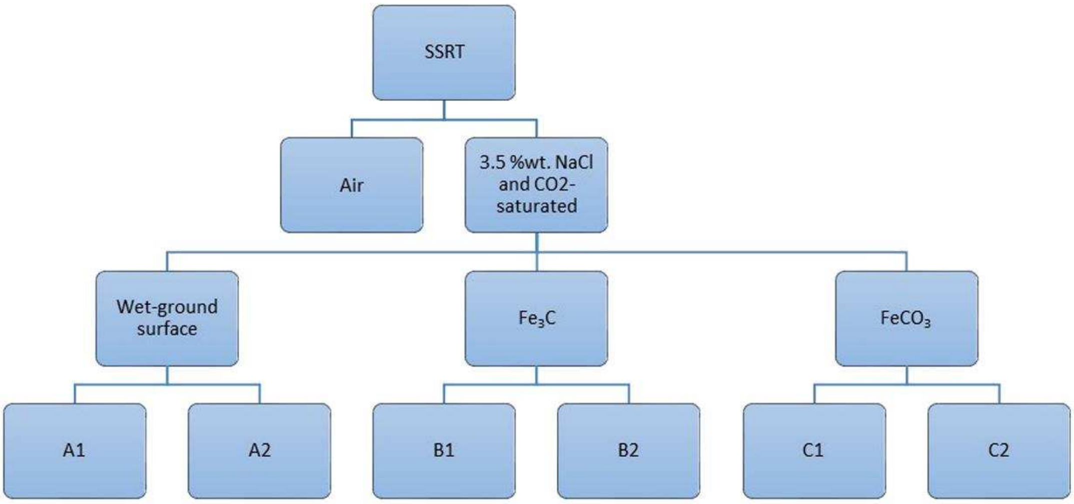

Figure 5: Flow sheet of experimental conditions adopted for SSRT.

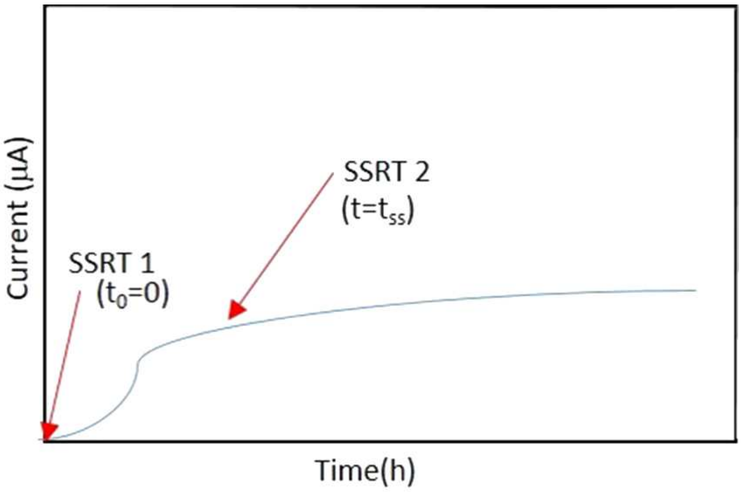

Figure 6: Schematic drawing of a hydrogen permeation curve to explain the conditions in which the loading is applied in the SSRT. SSRT1: t_0 = 0 defined from the hydrogen permeation test. The charging process begins when the hydrogen diffusion begins. SSRT2: Time (t = t_{ss}) required to reach the steady state hydrogen diffusion. Loading of SSRT starts after hydrogen saturation of the sample.

SSRT conditions can be summarised as:

- In air
- 3.5% NaCl solution and CO_2-saturated:
    - Wet-ground surface:

        - A1: Corresponding to t_0=0 defined on hydrogen permeation test. This condition implies that the loading process starts when hydrogen diffusion begins on the hydrogen permeation on the wet-ground surface specimen;
        - A2: Corresponding to time (t_{ss}) required to the steady state hydrogen diffusion. Loading of SSRT starts after hydrogen saturation of the specimen;
    - Fe_3C rich surface
        - B1: Corresponding to condition similar to defined for A1, but on the Fe_3C rich surface specimen;
        - B2: Corresponding to condition similar to defined for A2, but on the Fe_3C rich surface specimen;
    - $FeCO_3$ film surface
        - C1:Corresponding to condition similar to defined for A1, but on the $FeCO_3$ film surface specimen;
        - C2: Corresponding to condition similar to defined for A2, but on the $FeCO_3$ film surface specimen;

3.0. RESULTS AND DISCUSSION

3.1. Pre-filming experiments – film characterisation and electrochemical properties

3.1.1. Formation of the Fe_3C rich surface

Figure 7(a) shows the corrosion rate as a function of time for two repeated experiments for API 5L X65 carbon steel at 30°C and pH 3.8 in a CO_2-saturated 3.5 wt.% NaCl brine over 20 h exposure. A clear increase in corrosion rate is observed in both experiments which is attributed to the revealing of a Fe_3C network as a result of preferential dissolution of the ferrite phase within the steel microstructure [11]. General corrosion rate rises from approximately 1 mm/year to 1.3 mm/year. The ability of Fe_3C to enhance the corrosion rate of the steel lies in its conductive nature and the fact it is able to increase the rate of the cathodic reaction, through either the process of internal acidification, galvanic effects or a combination of both [12,4]. This galvanic effect is associated to the OCP (Figure 7(b)) shift to higher values occurring with increasing corrosion rate.

Corrosion morphology and surface composition after the experiment can be investigated by SEM analysis. The SEM images provided in Figures 7(c) and (d) confirm the preferential dissolution of the ferrite phase within the steel microstructure.

Ferrite-rich areas have receded and the ferrite-containing regions within the pearlite lamellar structure were preferentially dissolved, as shown in Figure 7(c).

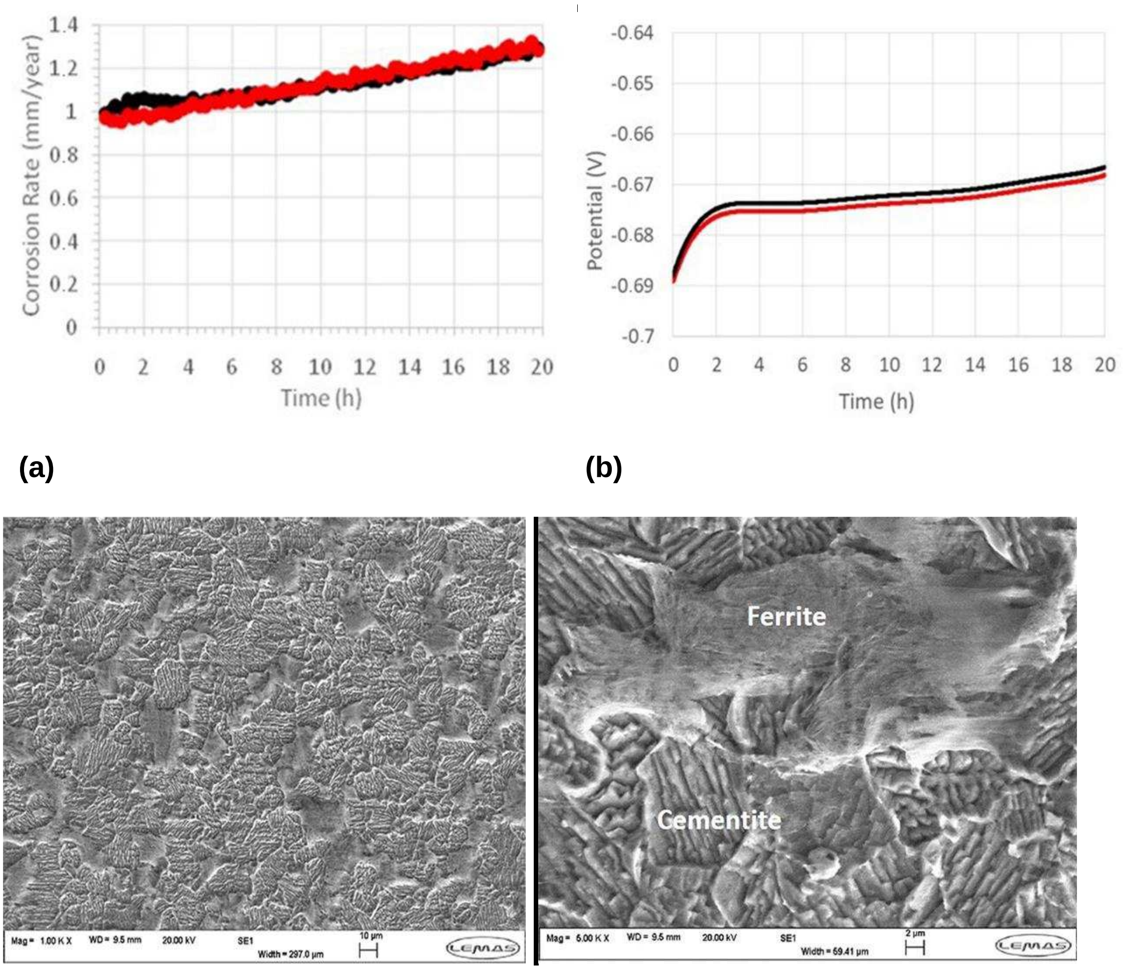

(a) (b)

(c) (d)

Figure 7: (a) Corrosion rate vs time for API 5L X65 carbon steel in a 3.5 wt.% NaCl CO_2-saturated brine over 20 h at 30^{o}C pH 3.8 (Stern-Geary coefficient of 13.0); (b) OCP vs time (c) and (d) SEM images of API 5L X65 surface after 20 h of exposure showing revealing of Fe_3C.

3.1.2. Formation of $FeCO_3$ film

Iron carbonate films were produced by immersion at 70^{o}C and pH 6.6 in a CO_2-saturated 3.5 wt.% NaCl brine. Figure 8(a) shows the corrosion rate as a function of time measured during this procedure for two repeated experiments, over 20 h of exposure. The corrosion rate of API 5L X65 reduces with time from a peak value of 1.3 mm/year to below 0.1 mm/year at the end of the $FeCO_3$ film formation experiment. The decrease in corrosion rate with time is associated with the surface blocking effect provided by the $FeCO_3$ crystals [8,13] which are clearly shown to cover the majority of the steel surface in the SEM image shown in Figure 8(b). The presence of $FeCO_3$ is confirmed in the XRD analysis as indicated in Figure 9, along with the pattern for the steel surface exposed to the pH 3.8/30ºC experiment where trace amounts of Fe_3C can be identified.

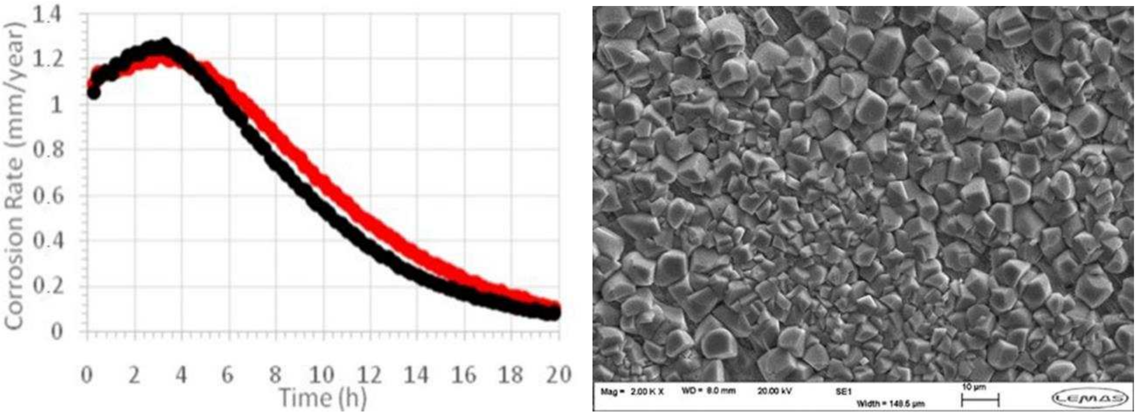

(a) **(b)**

Figure 8: (a) Corrosion rate vs time for API 5L X65 carbon steel in a 3.5 wt.% NaCl CO_2-saturated brine over 20 h at 70ºC pH 6.6 (Stern-Geary coefficient of 16.1); (b) SEM image of API 5L X65 surface after 20 h of exposure showing precipitation of $FeCO_3$.

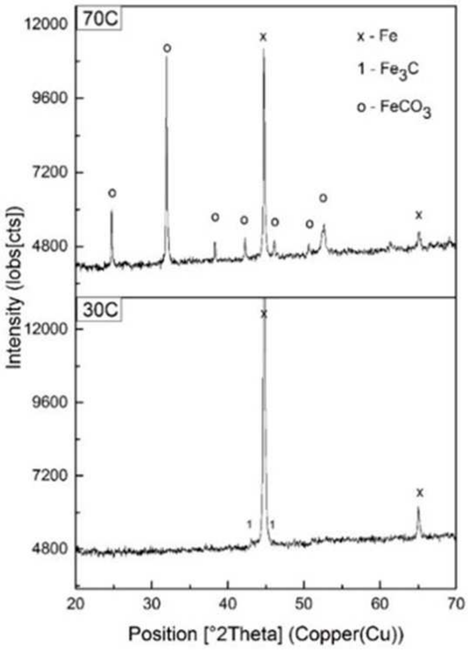

Figure 9: XRD patterns of API 5L X65 steel surfaces after exposure to a CO_2-saturated 3.5 wt.% NaCl solution at 70ºC/pH 6.6 and 30ºC/pH 3.8 for 20 h.

3.2. Cathodic polarisation characteristics of filmed interfaces

After the film formation process, each of the steel samples embedded in resin were immediately transferred into a CO_2-saturated 3.5 wt.% NaCl solution at pH 3.8 and room temperature to evaluate their cathodic polarisation characteristics which could then be correlated with the hydrogen permeation behaviour.

For all cathodic sweeps conducted with the filmed and wet-ground samples at room temperature, the OCP is in the range of -650 to -685 mV vs Ag/AgCl, with scan rate equal to 0.25 mV/s. Considering Figure 10, in the absence of Fe_3C or $FeCO_3$, the shape of the curve shows a mass transport limitation very close to the OCP. This has been shown to be attributed to the diffusion limited reduction of hydrogen ions at the steel surface. This behaviour has been discussed in literature and it has been shown by Remita et al. [14] that the cathodic current in this range is associated with the direct reduction of H^+ and a buffering effect from carbonic acid close to the steel surface. For more negative cathodic potentials, the dominant cathodic reaction becomes the reduction of water. Corresponding OCP in CO_2-saturated environment, equilibrium potential for hydrogen reduction reaction and H^+/H_2 driving force in each condition are listed on Table 2. From these data, it can be observed that the electrochemical driving force necessary for hydrogen reduction depends on the interface composition. In other words, electrode potentials measured in CO_2-saturated environment were always below the equilibrium potential H^+/H_2, based on Pourbaix diagram [15], corresponding to the system Fe/H_2O at 25 ℃. Then, it is possible to conclude that spontaneous hydrogen reduction would occur, from a thermodynamic point of view.

Table 2: Corrosion potentials in CO_2-saturated 3.5 wt.% NaCl solution in pH 3.8 for the different surface conditions, equilibrium potential for H^+/H_2 reduction reaction and H^+/H_2 driving force .

	pH	**OCP (V) after 20 h**	**Eq. Pot. H^+/H_2 (V)**	**H^+/H_2 Driving Force**
Wet-ground surface	3.8	-0.685	-0.432	0.253
Fe_3C		-0.665		0.233
$FeCO_3$		-0.650		0.218

From the cathodic polarisation curves is possible to observe that when the sample with Fe_3C present on the steel surface is inserted into the same test environment, there is a clear accentuation of the cathodic reaction in the diffusion-controlled potential range.

This is attributed by some authors to the ability of Fe_3C to provide a lower overpotential for the hydrogen reduction reaction [12,4].

From the same result, it can be concluded that the $FeCO_3$ film significantly reduces the cathodic reaction rate. This effect has been attributed to a surface blocking effect from $FeCO_3$ crystals, in other words, to their ability to act as a diffusion barrier, hindering the movement of electrochemically active species involved in the charge-transfer process [13,6].

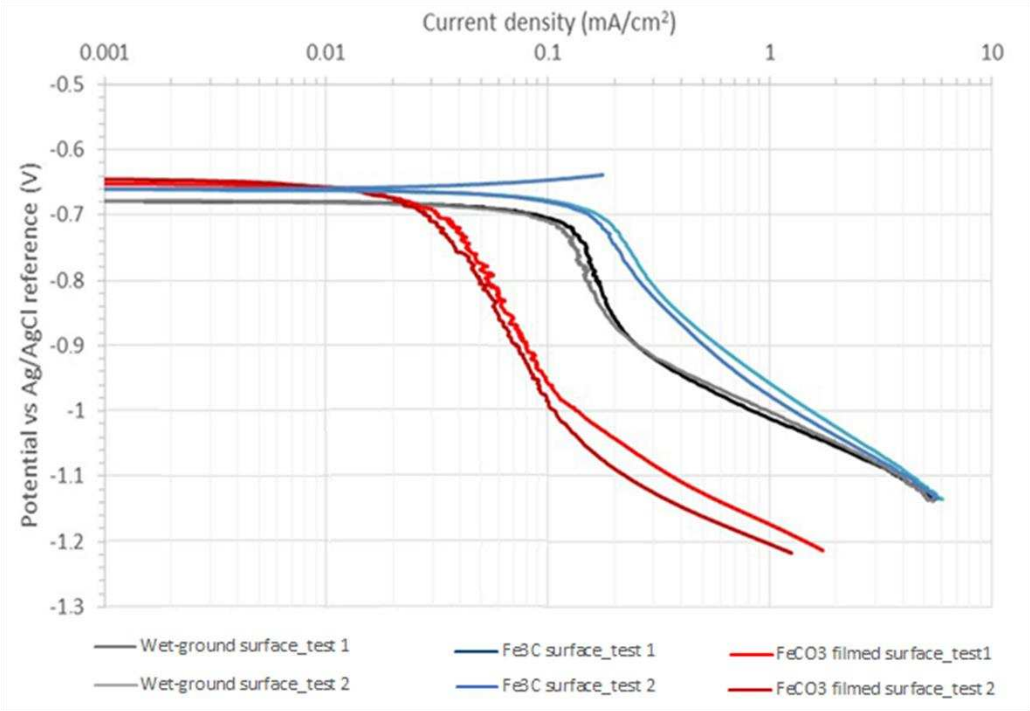

Figure 10: Cathodic polarisation scans performed on API 5L X65 steel samples in a CO_2-saturated 3.5 wt.% NaCl solution at room temperature and pH 3.8. Samples were either wet-ground or possessed a Fe_3C rich or $FeCO_3$ rich layer on the steel surface.

3.3. Hydrogen Permeation

The beginning of hydrogen permeation curves correspond to the current change at the moment in which the cathodic side is filled with CO_2-saturated 3.5 wt.% NaCl solution.

The effect of the different films on the hydrogen permeation current density is illustrated in Figure 11. The first observation is that hydrogen permeation occurs even in pure CO_2 systems. Because, when oxygen is removed from the system the OCP changes to a value below the equilibrium potential H/H^+ [16]. Consequently, it can be assumed that in CO_2-saturated solution, corrosion is associated to hydrogen reduction. This corroborates with the observations made by Plennevaux et al. [1], albeit with smaller permeation currents measured here due to the differences in sample thickness used. However, the values of current density are very low when compared to H_2S environments, as showed by Bueno et al [17], in which it was observed that thiosulphate ions added to the NS4 standard solution purged with CO_2 increased the hydrogen permeation of the API 5L X60 steel when compared to the permeation flux measured in NS4 standard solution. In addition, it was observed that the steel also presented hydrogen permeation in NS4 standard solution, that it was purged with CO_2, but in this condition, the permeation was lower than in NS4 solution plus thiosulphate ions.

Secondly, it is clear that the presence of the undissolved Fe_3C layer has a strong impact on the hydrogen permeation in the steel, raising the steady state current from that observed for the wet-ground steel surface from 0.2 $\mu A/cm^2$ to 0.8 $\mu A/cm^2$. This behaviour could be explained by the fact that Fe_3C rich surface accentuates the cathodic reaction in the diffusion limited region. Consequently the hydrogen reduction reaction would be facilitated at a lower potential, increasing the hydrogen permeation into the steel [12,4].

However, despite the ability of $FeCO_3$ to suppress the cathodic reactions in CO_2 system, the steady state hydrogen permeation current is slightly higher than that measured for the freshly polished steel surface. Although the uniform corrosion rate attenuation had been observed on $FeCO_3$ surface, the results indicate that occurred a small increase in hydrogen permeation current in this surface, in other words, this layer cannot act as a barrier for hydrogen diffusion and uptake.

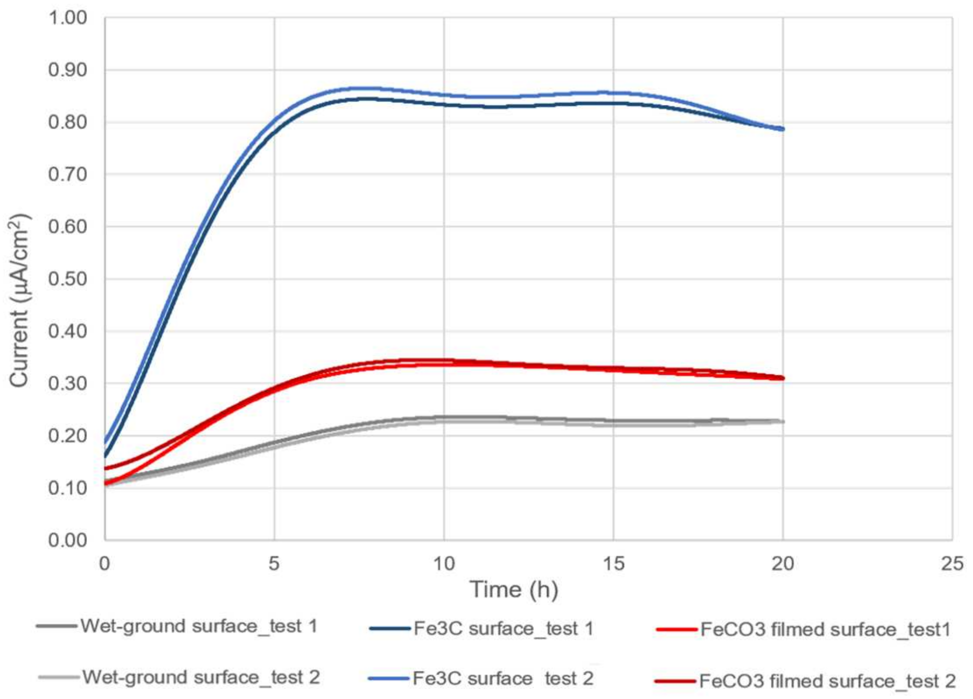

Figure 11: Hydrogen permeation curves performed on API 5L X65 samples in CO_2-saturated 3.5 wt.% NaCl solution at room temperature and pH 3.8. Samples were either wet-ground or possessed a Fe_3C rich or $FeCO_3$ rich layer on the steel surface.

Table 3 shows the parameters obtained from triplicate hydrogen permeation curves, such as steady state hydrogen flow (J_{ss}), effective hydrogen diffusivity (D_{eff}), permeability (P) and surface hydrogen concentration (C_H) on the cathodic side of sample, according ASTM G148 [18]. The surface hydrogen concentration on the cathodic side and the steady state hydrogen flow are higher for Fe_3C rich surface samples, as well as the permeability. However, effective hydrogen diffusivity is superior for the wet-ground surface.

Table 3: Parameters obtained from a triplicate of data hydrogen permeation curves, according to ASTM G148 [18].

Parameters **Test Condition**	**I_{ss} (μA)**	**$J_{ss} \times 10^{-12}$ (mol/cm^2.s)**	**$D_{eff} \times 10^{-6}$ (cm^2/s)**	**P x 10^{-12} (mol/cm.s)**	**$C_H \times 10^{-6}$ (mol/cm^3)**
Wet-ground_test 1	0.21	2.22	1.43	0.67	0.47
Wet-ground_test 2	0.23	2.34	1.48	0.70	0.47
Fe_3C_test 1	0.80	8.25	0.98	2.47	2.53
Fe_3C_test 2	0.79	8.22	1.01	2.47	2.44
$FeCO_3$_test 1	0.31	3.25	1.05	0.98	0.93
$FeCO_3$_test 2	0.31	3.25	1.00	0.98	0.98

I_{ss} is the steady state permeation current.

J_{ss} is the steady state hydrogen flow obtained from the Equation 5.

$J_{ss} = I_{ss}/(F.A)$ Eq. 5

Where, F is Faraday constant (96485 C/mol) and A is the useful area of sample (1 cm^2).

D_{eff} is the effective hydrogen diffusivity gotten from the Equation 6.

$D_{eff} = L^2/(6\ t_{lag})$ Eq. 6

Where, L is the thickness of sample and t_{lag} is the elapsed time to achieve 63% steady state flow.

P is the permeability obtained from the Equation 7.

$P = J_{ss}\ L$ Eq. 7

Finally, C_H is the surface hydrogen concentration on the cathodic side of the sample, obtained from Equation 8.

$C_H = (J_{ss}\ L)/D_{eff}$ Eq. 8

Diffusion is a process that depends on the time, therefore, the hydrogen amount carried inside the metal is also a function of time. This rate is expressed by the steady state hydrogen flow (J_{ss}) that is inversely proportional to the exposed area of metal. In hydrogen permeation tests, steady state hydrogen flow was lower on wet-ground surface. This can be explained by the higher exposed area on wet-ground surface condition. While on Fe_3C rich surface presented the highest hydrogen flow, it may happen because of the porosity of the pre-corroded surface, as confirmed by Mora-Mendoza and Turgoose (2002) [19] and Paolinelli et al (2008) [20] who showed that films of corrosion products formed below 40 ℃ in chloride environment containing CO_2 are porous. Meanwhile, on the $FeCO_3$ film surface an intermediate hydrogen flow was reached, probably due to the presence of some holes on the film that are preferential sites for hydrogen saturation and permeation. The exposed areas may be higher than one on Fe_3C rich surfaces. Yin (2009) [21] shows that at 70 ℃ thickness, porous and scattered $FeCO_3$ film is formed, ratifying the same structure of film formed in this study.

Effective hydrogen diffusivity (D_{eff}) is also known as diffusion coefficient. This property qualifies the propagation speed of hydrogen inside the metal, being the most important comparison parameter among metals. D_{eff} is higher in wet-ground surface than in Fe_3C rich and in $FeCO_3$ film surface, due to the thickness of sample that is smaller on the surface without film and to the higher facility of hydrogen to move through metal microstructure interstitially.

Permeability (P) is the maximum amount of hydrogen that crosses a metal of known thickness. Permeability was also higher in Fe_3C rich surface, since this parameter is dependent on the steady state hydrogen flow.

Hydrogen concentration (C_H) is related to the maximum concentration of absorbed hydrogen on the metal surface. Fe_3C rich surface presented higher hydrogen concentration as well as higher steady state hydrogen flow.

A statistical analysis was made in order to get the average and observe the data fluctuation in relation to the average of the parameters obtained from hydrogen permeation curves. Table 4 presents the average, standard deviation and variance of the steady state hydrogen flow, effective hydrogen diffusivity, permeability and surface hydrogen concentration on the cathodic side of sample from triplicate of hydrogen permeation tests. As indicated, all parameters present a low standard deviation, indicating that the data points tend to be close to the average, therefore confirming the reproducibility of the tests.

Table 4: Statistical analysis of the steady state hydrogen flow, effective hydrogen diffusivity, permeability and surface hydrogen concentration on cathodic side of sample.

	Average			**Standard Deviation**			**Variance**		
	Wet-ground surface	**Fe_3C**	**$FeCO_3$**	**Wet-ground surface**	**Fe_3C**	**$FeCO_3$**	**Wet-ground surface**	**Fe_3C**	**$FeCO_3$**
J_{ss} x 10^{-12} ($mol/cm^2.s$)	2.28	8.21	3.25	5.75 x10^{-2}	4.74 x10^{-2}	4.32 x10^{-3}	3.31 x10^{-3}	2.25 x10^{-3}	1.86 x10^{-5}
D_{eff} x 10^{-6} (cm^2/s)	1.67	1.01	1.06	6.23 x10^{-1}	3.40 x10^{-2}	7.37 x10^{-2}	3.89 x10^{-1}	1.15 x10^{-3}	5.44E x10^{-3}
P x 10^{-12} (mol/cm.s)	0.68	2.46	0.97	1.73 x10^{-2}	1.42 x10^{-2}	1.29 x10^{-3}	2.98 x10^{-4}	2.02 x10^{-4}	1.68 x10^{-6}
C_H x 10^{-6} (mol/cm^3)	0.45	2.44	0.92	1.81 x10^{-1}	9.53 x10^{-2}	6.39 x10^{-2}	3.28 x10^{-2}	9.08 x10^{-3}	4.08 x10^{-3}

A long term test was performed at OCP, in order to confirm the relation between surface composition and the hydrogen permeation. The test was carried out over 180 hours using the same cell displayed in Figure 3. It was observed during the first phase of the test, that the permeation current from the wet-ground surface, presented a low value, around 0.13 $\mu A/cm^2$, during the initial hours. After around 40 hours, in the second phase of the test, the permeation current increased until achieving a higher value, around 0.65 $\mu A/cm^2$, where it is kept near the steady state. This second phase consists of a Fe_3C enriched surface. Permeation current on the anodic side, and the OCP on the cathodic side were continuously registered. Figure 12 shows hydrogen permeation curves and Figure 13 shows the OCP for the tests performed during 180h. It is observed that the increase of permeation current is related to the OCP evolution that changes due to Fe_3C surface enrichment on cathodic side of the sample, along the test. This result is in accordance to the results of separate experiments that indicate a low permeation current on wet-ground steel surface, and a high permeation current value on Fe_3C pre-corroded surface.

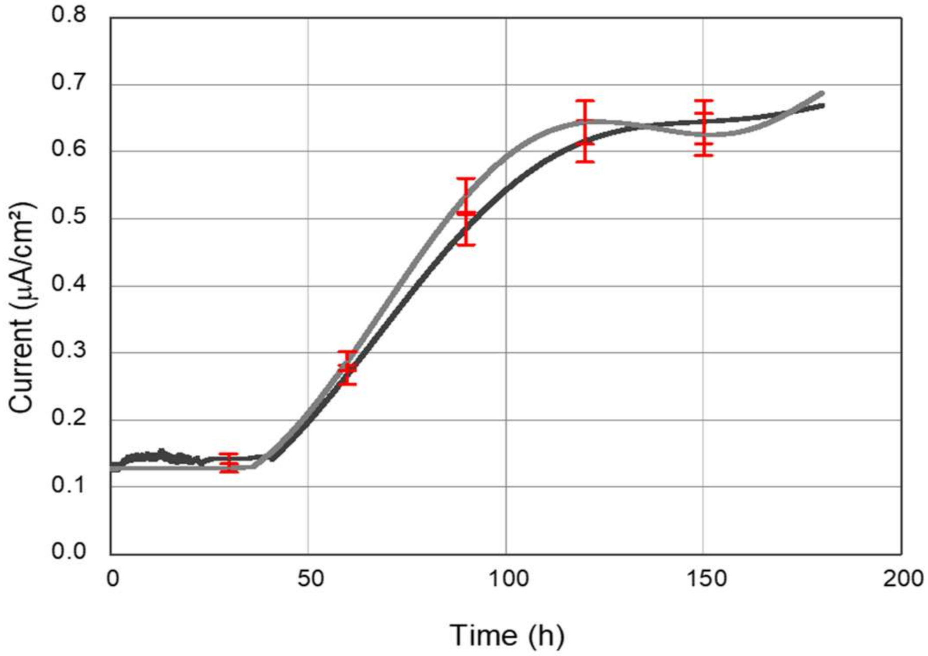

Figure 12: Hydrogen permeation test curves performed on API 5L X65 samples in CO2-saturated 3.5 wt.% NaCl solution at room temperature and pH 3.8. Wet-ground surface samples were exposed for 180h and the Fe_3C enrichment on the steel surface occurred during the test.

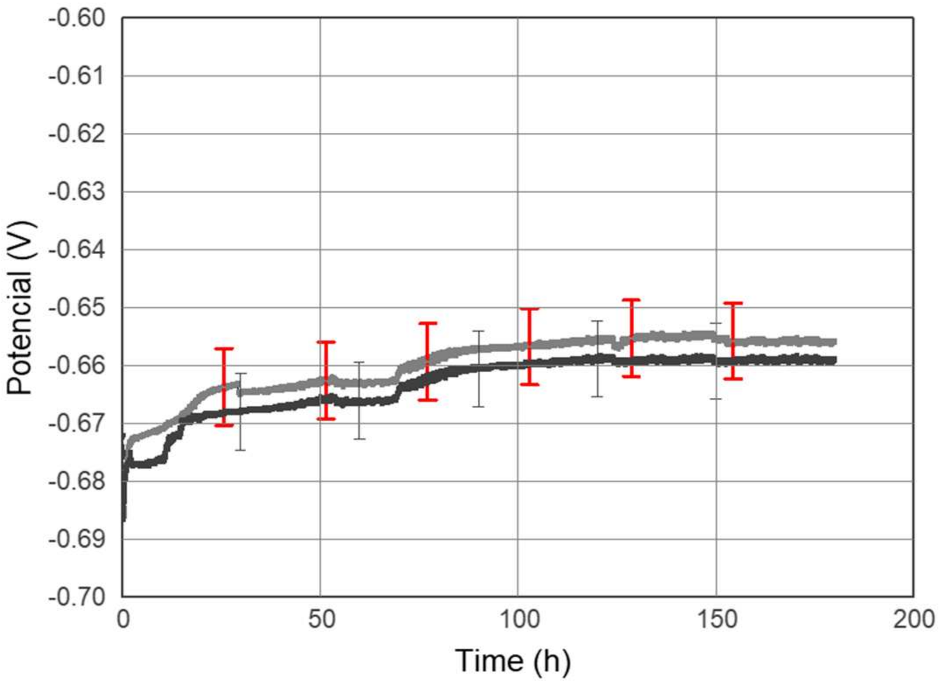

Figure 13: Potentiometry curves performed on API 5L X65 samples in CO_2-saturated 3.5 wt.% NaCl solution at room temperature and pH 3.8. Samples were wet-ground surface were exposed for 180h. There was Fe_3C enrichment on the steel surface during the test.

3.4 Slow Strain Rate Tests

SSRTs were performed to assess the influence of the CO_2-saturated 3.5 wt.% NaCl solution on the mechanical resistance of the API 5L X65 steel at room temperature**.** Stress versus time curves obtained and the parameters obtained from SSRT in air and in CO_2-saturated solution are shown in Figure 14, Table 5 and Table 6, respectively.

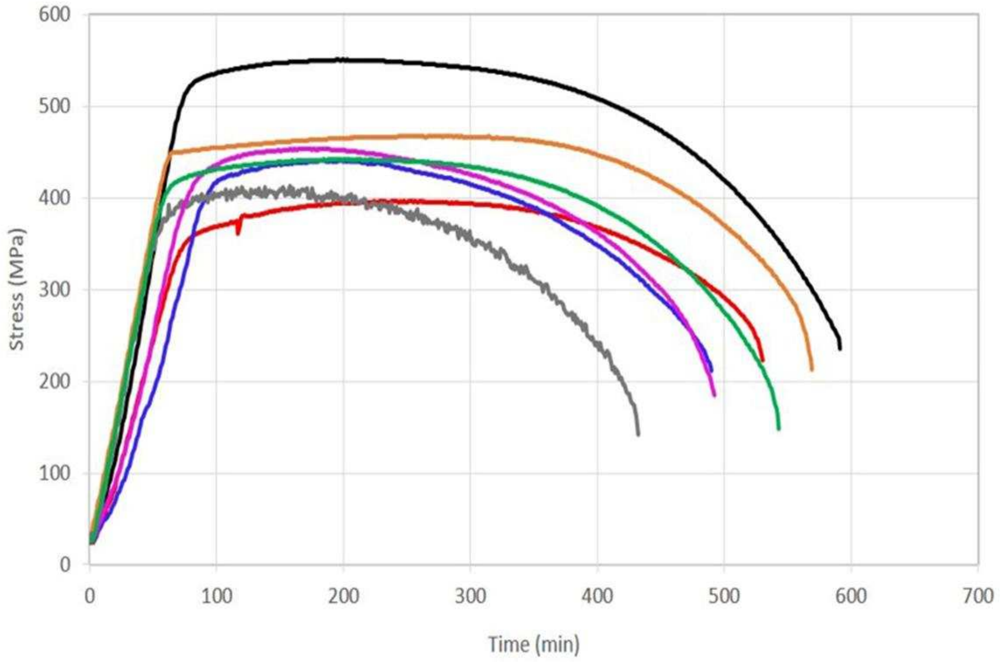

Figure 14: Stress versus time curves of an API 5L X65 steel in CO_2-saturated 3.5 wt. % NaCl solution under the strain rate $4.7x10^{-6}$ s^{-1}.

Table 5 presents a statistical analysis of the average, standard deviation and variance of reduction in area (RA) and time-to-failure (TTF) from triplicate of data of each test condition. It is possible to observe that the parameters obtained from each test condition have a low standard deviation, confirming the reproducibility of the tests.

Table 5: Statistical analysis of reduction in area (RA) and time-to-failure (TTF).

	Average		**Standard Deviation**		**Variance**	
	RA%	**TTF (h)**	**RA%**	**TTF (h)**	**RA%**	**TTF (h)**
Air	87.083	9.68	1.189	0.16	1.413	0.026
A1	79.156	8.16	0.238	1.02	0.057	1.039
A2	76.059	7.74	1.284	0.38	1.650	0.14
B1	69.906	9.66	0.503	0.17	0.253	0.028
B2	65.955	7.78	1.176	0.78	1.383	0.61
C1	75.240	8.24	0.658	0.52	0.433	0.27
C2	62.657	9.23	1.610	0.21	2.591	0.045

Table 6 shows the ratio of reduction in area (RRA) for the API 5L X65 steel determined from the ratio between each test in corrosive environment and in the test in air. According to ASTM G129 standard [10], the susceptibility to environment assisted cracking hydrogen of the materials in SSRT can be expressed by the RRA. This index corresponds to the ratio of the reduction in area determined for the material in the test environment (RA_e) and the corresponding value determined in the control environment (RA_c), i.e., in air. When this ratio is below one, the material is considered susceptible to embrittlement and when the ratio is close to one, the material is environment resistant. The same ratio is validate for time-to-failure (RTTF) [22].

Table 6: Ratio of reduction in area (RRA) and ratio of time-to-failure (RTTF) of the API 5L X65 steel.

		$RRA=(RA_e/RA_c)$	$RTTF=(TTF_e/TTF_c)$
Wet-ground surface	**A1**	0.909	0.84
	A2	0.873	0.80
Fe_3C	**B1**	0.803	0.99
	B2	0.757	0.80
$FeCO_3$	**C1**	0.864	0.85
	C2	0.720	0.95

The first observation is that the API 5L X65 has yield strength and tensile strength around 505 MPa and 536 MPa, respectively. The average of the time-to-failure (TTF) obtained in test in air was approximately 9 hours and 40 minutes, as shown in Table 5.

Reduction in area and time-to-failure were obtained from SEM analyses and from the stress versus time curves, respectively. The mechanical properties of the material were affected in all test conditions. However, it has been observed a less significant reduction in TTF in tests carried out on Fe_3C rich surface, B1 condition; and on $FeCO_3$ film surface, C2 condition, when compared to the on wet-ground surface, condition A1 (Table 5). Moreover, the elastic limit was less in all test conditions in solution compared to the air test, as shown in Figure 14.

Table 5 also show loss of ductility of the material when tested on wet-ground surface in condition A1, since the reduction in area decreased from approximately 87% in air to around 79% in solution, exhibiting RRA of 0.909 (Table 6). In the A2 condition, a drop in the TTF and in the RA were also observed, indicating RRA of 0.873. However, the loss of ductility observed was lower than a similar material in an environment containing H_2S [17,19]. On the other hand, a higher grade steel, API 5L X80 in a H_2S environment exhibited a reduction in area of 64% in air and 27% in solution, corresponding to RRA equal to 0.472 [22]. These data suggest the possibility of a more severe embrittlement of higher mechanical resistance steels in pure CO_2 environments.

The reduction of the parameters defined by ASTM G129 standard [10] is primarily attributed to the influence of hydrogen, as suggested by the hydrogen permeation tests carried out. It is important to observe that the OCP of steel increased on Fe_3C rich surfaces indicating that the driving force for hydrogen reduction decreases but the hydrogen current permeation increases. Based on this assumption, deleterious effects of hydrogen were observed in tests carried out on Fe_3C rich steel surfaces. Loss of ductility were observed in conditions B1 and B2. However, the embrittlement effect was more severe in condition B2, due to the lower elastic regime observed in this condition, besides lower values of TTF and RRA parameters. Elastic limit reduction can be partially induced by localized dissolution process. Stress concentration would drive to the decreasing of the mechanical resistance of the material in the corrosive environment.

Similar effect was observed on the SSRT carried out with $FeCO_3$ rich steel samples. The elastic regime was also lower in both tests performed on $FeCO_3$ film surfaces. Lower reduction in area was observed, especially in tests in the C2 condition. On the other hand, TTF in the C2 condition was close to the TTF obtained in air, while in C1 condition was much lower. According to the parameters obtained from hydrogen permeation tests on $FeCO_3$ rich samples, hydrogen embrittlement contribution would be lower. Considering the loss of mechanical properties of the steel, as presented in Table 5, another effect that should be considered is the rupture of the $FeCO_3$ film driving to a more critical localized corrosion incidence. This assumption is supported by the corrosion rates measured for the API 5L X65 steel without and with the presence of the $FeCO_3$ film, 1.3 mm/year and 0.1 mm/year, respectively.

The ratios of reduction in area presented in Table 6 ratify the embrittlement induced by the corrosive environment, showing loss of ductility in the CO_2-saturated environment in all the studied conditions. To confirm that the ductility of the steel decreases, but less than in H_2S environment, this study can be compared with Bueno et al [17], that showed that API 5L X60 steel exhibited a loss of ductility due to hydrogen embrittlement in the modified standard solution NS4. The ratio of reduction in area obtained was 0.6912 in the NS4 solution and 0.656 in NS4 containing H_2S.

3.5 Scanning Electron Microscopy Analysis (SEM)

Scanning Electron Microscope (SEM) analysis of fracture and lateral surfaces of SSRT samples after testing is a basic requirement to achieve a better interpretation of the material behaviour in air and in CO_2-saturated solutions.

Fracture surfaces and final diameters of the steel after testing are shown, respectively, in air, Figures 15 (a) and (b); on Fe3C rich surface, condition B2, Figures 15 (c) and (d); and on $FeCO_3$ filmed surface, condition C2, Figures 15 (e) and (f). The sample of Figures 15 (a) and (b), test in air, shows an elliptical shape and the diameter must be obtained by the measurement of both axes of the fracture surface. Likewise, the measurements were obtained for the other samples, as shown on Figures 15 (c) and (d) and Figures (e) and (f) corresponding to the most severe conditions observed for the material tested in CO_2 solutions. The loss of ductility is evident from the comparison of the diameters in air and in solution. It is noted that there were higher necking down for tests in air than in solutions, particularly in B2 and C2 conditions. It implies that the reduction in area, and consequently ductility, was lower in these conditions. These data complies with the data obtained from SSRT (Table 5), showing that the steel presented ductile fracture in air, with plastic deformation considerable, cup-and-cone morphology. However, in test conditions B2 and C2 there was a significant loss of ductility due to hydrogen embrittlement. Bueno et al. [16] also studied a ferrite-perlite microstructure steel, which also presented a similar ductile fracture surface, with great reduction in area in the SSRTs carried out in air, while in NS4 solution with bubbling of CO_2 presented to decrease of reduction in area, therefore the loss of mechanical properties.

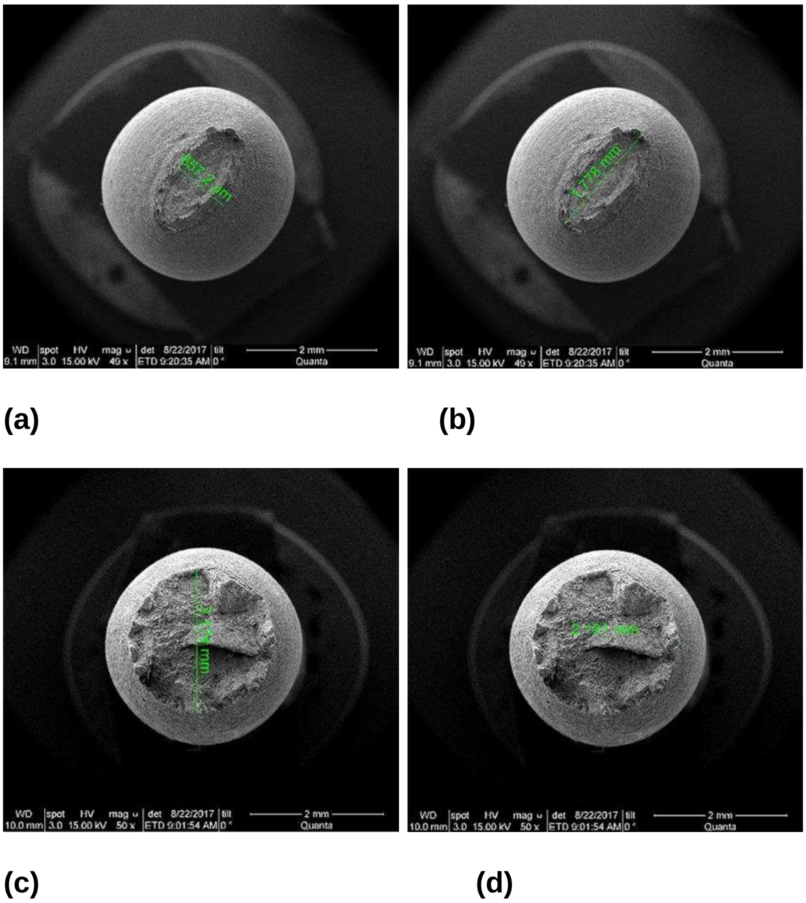

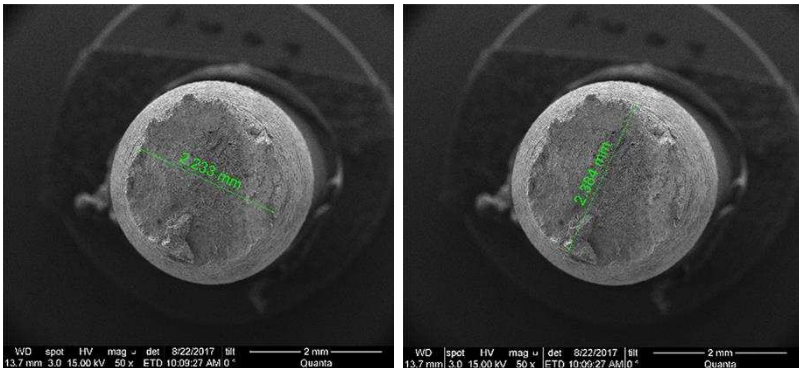

(e) **(f)**

Figure 15: SEM: Fracture surfaces and measured diameters of the API 5LX65 steel after SSRTs in air and in CO_2-saturated environment. (a) and (b) Air. (c) and (d) Fe_3C rich surface, in CO_2-saturated environment condition B2. (e) and (f) $FeCO_3$ filmed surface, in CO_2-saturated environment condition C2. Magnification: 50x.

Figure 16 shows the aspect of the lateral surface of steel after SSRT. Figures 16 (a), (b) and (c) are related to the tests in air and in CO_2-saturated environment in conditions B2 and C2, respectively. Figure 16(a) confirms the significant necking down, of the material tested in air. The similar lateral surfaces of the samples tested in B2 condition presents a reduced necking down, thus a lower reduction in area, evidencing loss of ductility and embrittlement of the steel, shown on Figure 16(b). Loss of ductility in condition C2 was also confirmed, due to the similar reduced necking down, as noticed in Figure 16(c) and the presence of secondary micro-cracks on the lateral surface close to the necking down region. Secondary surface cracking is commonly associated to anodic dissolution contribution and could be responsible to the reduction of the elastic limit. This mechanisms can occur under the conjoint influence of anodic dissolution, stress concentration and hydrogen uptake. The presence of these micro-cracks implies that the fracture mechanism during SSRT is governed by the interaction between hydrogen effects and localized corrosion. The presence of surface films, such as $FeCO_3$, can drive to more critical localised corrosion incidence due to the rupture of the film, induced by the dynamic strain, forming preferential sites for localized corrosion. In many cases of Environment Assisted Cracking, both anodic dissolution and hydrogen effects are involved and interact with the localized crack-tip plasticity. Parkins et al. [23] confirms, in his study, that SCC process is characterized by the conjoint effect of anodic dissolution and hydrogen embrittlement. Therefore, it is possible to conclude that the tests carried out in C2 condition, Figure 16 (c), were more aggressive than tests performed in B2 condition, Figure 16 (b), due to the presence of secondary micro-cracks. Such cracking mechanism was not observed on the lateral surface of the Fe_3C rich surface samples, where a uniform corrosion morphology was expected. Moreover, according to Vancostenoble et al. [24], although the precipitated $FeCO_3$ at the surface acts as a protective film reducing the corrosion rate, in presence of environmental fluctuations and/or stress and strain, this protective layer can be damaged, inducing fracture and leading to SCC or Hydrogen Embrittlement. Besides that, external cracking of pipelines is consequence of complex interactions between physical and chemical factors [25].

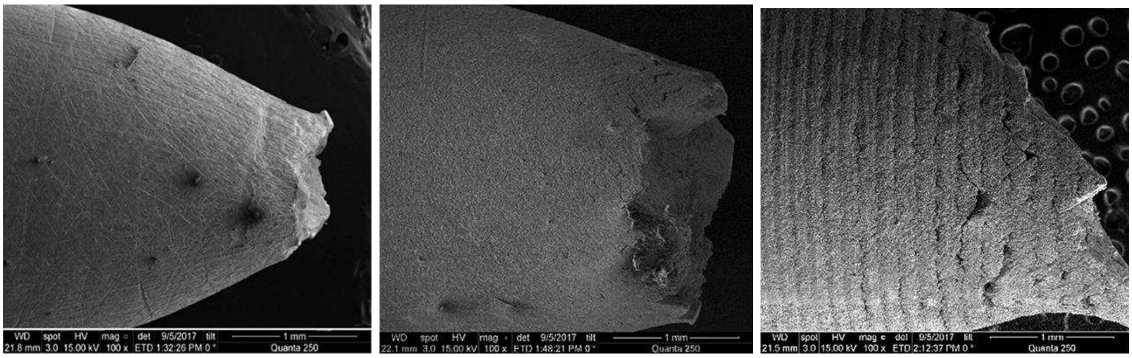

(a) (b) (c)

Figure 16: SEM: Lateral surfaces of the carbon steel after SSRTs in air and in CO_2-saturated environment. (a) Air. (b) Fe_3C rich surface, condition B2. (c) $FeCO_3$ filmed surface, condition C2. Magnification: 100x.

Steel tested in air presented ductile fracture mechanism of cup-and-cone type, in which is observed the coalescing of micro-porosity, dimples, in center and in the edges of the fracture surface, Figure 17(a) and (b). This fracture surface presents the three characteristics of ductile fracture, which are: considerable plastic deformation in the region of ductile fracture; the applied shear stress exceeds the shear strength before any other fracture modes can occur; and the appearance of the ductile fracture is matte and fibrous, that it is caused by the deformation at the fracture surface.

Figures 17 (c) and (d) show fracture surface of carbon steel after test on Fe_3C rich surface, in CO_2-saturated environment (B2 condition). Fracture surface exhibits a mixed appearance, ductile and brittle, with fewer dimples and shallower in the center of the sample and with an internal crack in the cross section. This exposes a fracture process characterized by a transgranular cracking morphology, with the edges of the fracture surface presented brittle behaviour by cleavage, evidencing loss of ductility of the material. Kellen et al. [26], in similar study, suggested that this type of crack is usually associated with the recombination of the hydrogen atoms, previously in solid solution, to form hydrogen molecules at microstructural interfaces.

In Figures 17(e) and (f) are observed images of sample after test on $FeCO_3$ film surface, C2 condition. Fracture surface presents few and shallow dimples on the middle of sample. Moreover, the edges of fracture surface also showed the brittle behaviour, with bright and faceted appearance, confirming the transgranular cracking morphology. So, a mixed fracture morphology was observed, featuring both brittle fracture by cleavage and ductile fracture by dimples, confirming the hydrogen embrittlement of the steel.

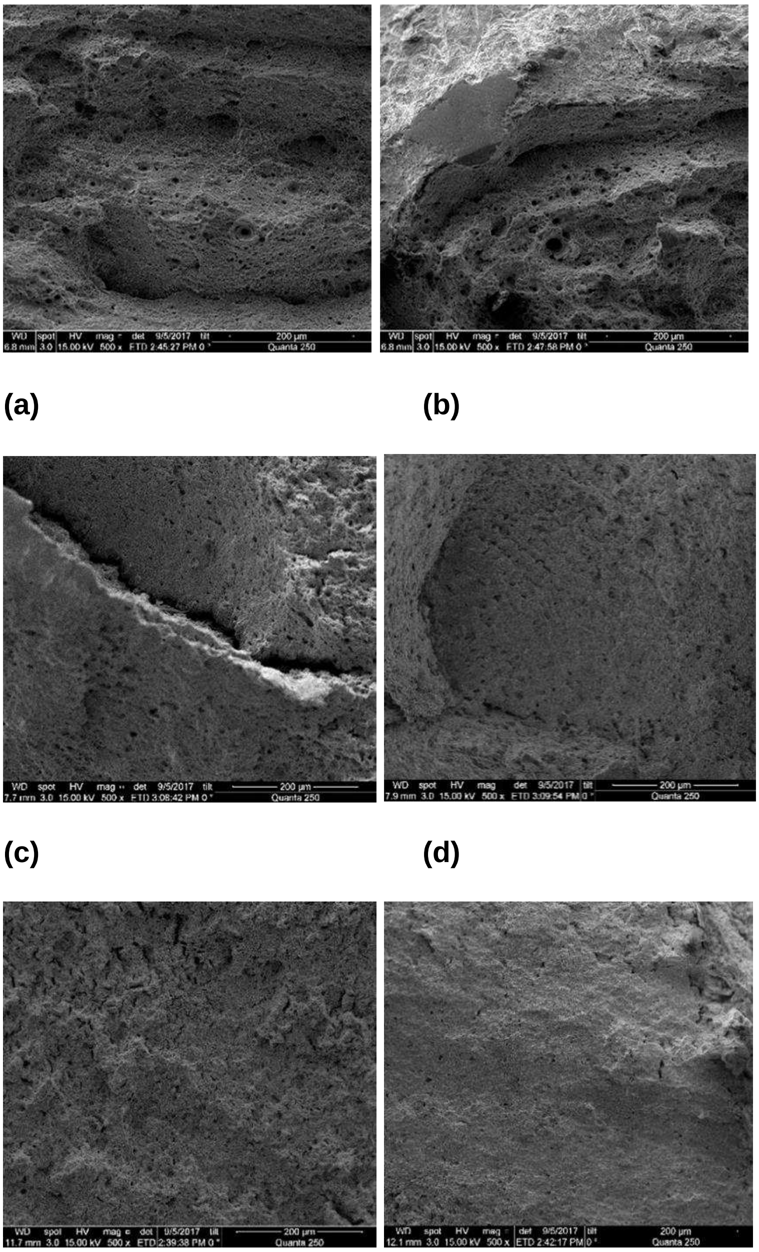

(a) **(b)**

(c) **(d)**

(e) **(f)**

Figure 17: SEM: Fracture surfaces of the carbon steel after test in air and in B2 and C2 conditions, respectively. Air: (a) Center; (b) Edge. Fe_3C rich surface, condition B2: (c) Center; (d) Edge. $FeCO_3$ filmed surface, condition C2: (e) Center; (f) Edge. Magnification: 500x.

Images obtained from SEM analysis showed the behaviour of the carbon steel after SSRT in air and in the two conditions that presented the higher loss of ductility, it corroborates the results showed previously, in which CO_2-saturated environment generates hydrogen that weakens the material in the conditions studied. Furthermore, Fe_3C and $FeCO_3$ film surfaces can induce a higher hydrogen embrittlement, mainly if in the B2 and C2 conditions, respectively, in which the material exhibited higher loss of ductility, thus higher hydrogen embrittlement, assisted by anodic dissolution in some specific surface conditions.

3. CONCLUSIONS

1. It was concluded that the API 5L X65 steel is susceptible to environment assisted cracking in pure CO_2 solution. The loss of mechanical resistance mechanism is driven by hydrogen that permeates in API 5L X65 steel. This conclusion is supported by the results obtained from Slow Strain Rate tests and Hydrogen Permeation tests. Nevertheless, the data obtained suggest a less critical detrimental effect than the one observed for the same material in H_2S environments.
2. The extent of the embrittlement effect depends on the steel surface composition. The presence of Fe_3C layer increases the hydrogen permeation in the steel, since it accentuates the cathodic reaction in the diffusion limit region, so that the hydrogen reduction reaction is facilitated in a lower potential, increasing the hydrogen permeation into the steel. Consequently is possible to conclude that a precorroded carbon steel interface in pure CO_2 environment increase the susceptibility to hydrogen uptake and embrittlement.
3. The steady state permeation current is not reduced in $FeCO_3$ filmed surface in comparison with the freshly polished steel surface, despite the ability of $FeCO_3$ to attenuate the cathodic reactions in the CO_2 system. Probably due to the presence of some holes in the $FeCO_3$ layer, that facilitates the hydrogen saturation, favouring the hydrogen diffusion through the steel surface.

4. In the long hydrogen permeation test at OCP, in which a pre-corrosion was performed together with hydrogen permeation test, it was observed that when Fe_3C was formed on the steel surface an OCP shift for higher values was observed. Moreover, the increase of hydrogen current was registered after the Fe_3C enrichment on the surface, reaching a higher steady state for the hydrogen current density. This result confirms the correlation between precorrosion in CO_2 and hydrogen diffusion.
5. The parameters obtained from SSRT, such as the reduction in area (RA) and time-to-failure (TTF) decreased at every CO_2 environment test conditions. The elastic limit reduction was also registered as an indication of detrimental effect of the CO_2 environment, assisted by the formation of secondary surface micro-cracks in $FeCO_3$ rich interface steel. Anodic dissolution and stress concentration plays an important role on this process.
6. SEM images showed the fracture of samples after test in air and in B2 and C2 conditions and support the results previously showed, that CO_2-saturated environment generates hydrogen that promotes the embrittlement in the carbon steel. Furthermore, Fe_3C and $FeCO_3$ film surfaces can induce a higher hydrogen embrittlement if in the B2 and C2 conditions, respectively, when the material exhibited higher loss of ductility.

ACKNOLEGMENTS

The authors would like to acknowledge the support provided by CNPq and Shell.

REFERENCES

[1] Plennevaux, C., Kittel, J., Frégonese, M., Normand, B., Ropital, F., Grosjean, F. and Cassagne, T. (2013). Contribution of CO_2 on hydrogen evolution and hydrogen permeation in low alloy steels exposed to H_2S environment. Electrochemistry Communications, 26, 17-20. DOI: 10.1016/j.elecom.2012.10.010

[2] Crolet, J.L. and Maisonneuve, G. (2000). Construction of a universal scale of severity for hydrogen cracking. Proceedings of NACE Corrosion 2000. Paper n°127. ISBN: 00127 2000 CP.

[3] Crolet, J.L. and Bonis, M.R. (2001). Revisiting hydrogen in steel. Part I: Theoretical aspects of charging, stress cracking and permeation. Proceedings of NACE Corrosion 2001. Paper n° 67. ISBN: 01067 2001 CP.

[4] Crolet, J.L., Thevenot, N. and Nesic, S. (1998). Role of Conductive Corrosion Products in the Protectiveness of Corrosion Layers. Corrosion, 54(3), 194-203. DOI: 10.5006/1.3284844

[5] Pessu, F., Barker, R. and Neville, A. (2015). The influence of pH on localized corrosion behavior of X65 carbon steel in CO_2-saturated brines. Corrosion, 71(12), 1452-1466. DOI: 10.5006/1770

[6] Barker, R., Hua, Y. and Neville, A. (2017). Internal corrosion of carbon steel pipelines for dense-phase CO_2 transport in carbon capture and storage (CCS) – a review. International Materials Reviews, 62(1), 1-31. DOI: 10.1080/09506608.2016.1176306

[7] Nordsveen, M., Nešic, S., Nyborg, R. and Stangeland, A. (2003). A mechanistic model for carbon dioxide corrosion of mild steel in the presence of protective iron carbonate films—part 1: theory and verification. Corrosion, 59(5), 443-456. DOI: 10.5006/1.3277576

[8] Hua, Y., Barker, R., Charpentier, T., Ward, M. and Neville, A. (2015). Relating iron carbonate morphology to corrosion characteristics for water-saturated supercritical CO_2 systems. The Journal of Supercritical Fluids, 98, 183-193. DOI: 10.1016/j.supflu.2014.12.009

[9] NACE Standard TM0198 (2016). Slow strain rate test method for screening corrosion-resistant alloys for stress corrosion cracking in sour oilfield service. ISBN: 1-57590051-3

[10] ASTM G129–95 (2000). Slow Strain Rate Testing to Evaluate the Susceptibility of Metallic Materials to Environmentally Assisted Cracking. DOI: 10.1520/G0129-00

[11] Farelas, F., Galicia, M., Brown, B., Nesic, S. and Castaneda, H. (2010). Evolution of dissolution processes at the interface of carbon steel corroding in a CO_2 environment studied by EIS. Corrosion Science, 52(2), 509-517. DOI:10.1016/j.corsci.2009.10.007

[12] Nesic, S., Thevenot, N., Crolet, J. L. and Drazic, D. M. (1996). Electrochemical properties of iron dissolution in the presence of CO_2 - Basics revisited. NACE Corrosion Conference 1996, Houston, TX (United States). Proceedings of NACE Corrosion 1996. Paper n°3. ISBN: 96003 1996 CP

[13] Dugstad, A., Hemmer, H. and Seiersten, M. (2001). Effect of steel microstructure upon corrosion rate and protective iron carbonate film formation. Corrosion, 57(4), 369-378. DOI: 10.5006/1.3290361

[14] Remita, E., Tribollet, B., Sutter, E., Vivier, V., Ropital, F., and Kittel, J. (2008). Hydrogen evolution in aqueous solutions containing dissolved CO_2: quantitative contribution of the buffering effect. Corrosion Science, 50(5), 1433-1440. DOI: 10.1016/j.corsci.2007.12.007

[15] Pourbaix, M. Atlas of Electrochemical Equilibria in Aqueous Solution, 1st ed.; Pergamon Press: Bristol, UK, 1966.

[16] Bueno, A.H.S., Moreira, E.D., Siqueira, P. and Gomes, J.A.C.P. (2014). Evaluation of stress corrosion cracking and hydrogen embrittlement in an API grade steel. Engineering Failure Analysis, 33, 163-175. DOI: 10.1016/j.engfailanal.2013.11.012

[17] Bueno, A.H.S., Moreira, E.D., Siqueira, P. and Gomes, J.A.C.P. (2014). Effect of cathodic potential on hydrogen permeation of API grade steels in modified NS4 solution. Materials Science & Engineering A 597, 117-121. DOI: 10.1016/j.msea.2013.12.033

[18] ASTM G148–97 (2011). Evaluation of hydrogen uptake, permeation and transport in metals by an electrochemical technique. DOI: 10.1520/G0148-97R11

[19] Mora-Mendoza, J. L.; Turgoose, S. (2002). Fe_3C influence on the corrosion rate of mild steel in aqueous CO_2 systems under turbulent flow conditions. Corrosion Science, v. 44. p.1223-1246, 2002. DOI: 10.1016/S0010-938X(01)00141-X

[20] Paolinelli, L. D., Pérez, T., Simison, S. N. (2008). The effect of pre-corrosion and steel microstructure on inhibitor performance in CO_2 corrosion. Corrosion Science, v. 50, p. 2456-2464, 2008. DOI: 10.1016/j.corsci.2008.06.031

[21] Yin, Z. F.; Feng, Y.R., Zhao, W.Z., Bai, Z.Q., Lin, G.F. (2009). Effect of temperature on CO_2 corrosion of carbon steel. Surf. Interface Anal, v. 41, p. 517-523, 2009. DOI: 10.1002/sia.3057

[22] Ballesteros, A.F., Gomes, J.A.C.P. and Bott, I.S. (2010). Study of the susceptibility of API 5L X80 girth welds to sulphide stress corrosion cracking and hydrogen embrittlement". Proceedings of the 8th International Pipeline Conference, IPC2010-31243. DOI: 10.1115/IPC2010-31243

[23] Parkins, R.N., Blanchard, W.K. and Delanty, B.S. (1994). Transgranular stress corrosion cracking of high-pressure pipelines in contact with solutions of near neutral pH. Corrosion, Vol. 50, no. 5, pp. 394-408. DOI: 10.5006/1.3294348

[24] Vancostanable, A., Duret-Thual, C., Bosh, C., Delafosse, D. (2014). Stress Corrosion Cracking of ferrito-pearlitic steel in aqueous environment containing dissolved CO_2. NACE Corrosion Conference 2014, Houston, TX (United States). NACE International, pp. ISBN 4321 2014 CP, 2014.

[25] Mohtadi-Bonab, M.A., Szpunar, J.A., Razavi-Tousi S.S. (2013). A comparative study of hydrogen induced cracking behavior in API 5L X60 and X70 pipeline steels. Engineering Failure Analysis. Vol. 33, p. 163-175. DOI: 10.1016/j.engfailanal.2013.04.028

[26] Kellen, R.S.L., Bott, I.S., Ponciano, J.A. (2015). Laboratory Investigation of Environmentally Induced Cracking of Api-X70 and X80 Pipelines Steels. 24° OMAE. June, 2005. DOI: 10.1115/OMAE2005-67560

List of Captions

Figures

Figure 1: Microstructure ferritic-pearlitic of API 5L X65 steel

Figure 2: Schematic of test cell for electrochemical measurements during Fe_3C and $FeCO_3$ film formation.

Figure 3: Schematic drawing of Devanathan-Stachurski cell for hydrogen permeation tests. Cathodic side to the left filled with CO_2-saturated 3.5 wt.% NaCl solution. Anodic side to the right filled with 1M NaOH.

Figure 4: Schematic drawing of cell used in the slow strain rate tests

Figure 5: Flow sheet of experimental conditions adopted for SSRT.

Figure 6: Schematic drawing of a hydrogen permeation curve to explain the conditions in which the loading is applied in the SSRT. SSRT1: t0 = 0 defined from the hydrogen permeation test. The charging process begins when the hydrogen diffusion begins. SSRT2: Time ($t = t_{ss}$) required to reach the steady state hydrogen diffusion. Loading of SSRT starts after hydrogen saturation of the sample.

Figure 7: (a) Corrosion rate vs time for API 5L X65 carbon steel in a 3.5 wt.% NaCl CO_2-saturated brine over 20 h at 30 ℃ pH 3.8 (Stern-Geary coefficient of 13.0); (b) OCP vs time (c) and (d) SEM images of API 5L X65 surface after 20 h of exposure showing revealing of Fe_3C.

Figure 8: (a) Corrosion rate vs time for API 5L X65 carbon steel in a 3.5 wt.% NaCl CO_2-saturated brine over 20 h at 70 ℃ pH 6.6 (Stern-Geary coefficient of 16.1); (b) SEM image of API 5L X65 surface after 20 h of exposure showing precipitation of $FeCO_3$.

Figure 9: XRD patterns of API 5L X65 steel surfaces after exposure to a CO_2-saturated 3.5 wt.% NaCl solution at 70 ℃/pH 6.6 and 30 ℃/pH 3.8 for 20 h.

Figure 10: Cathodic polarisation scans performed on API 5L X65 steel samples in a CO_2-saturated 3.5 wt.% NaCl solution at room temperature and pH 3.8. Samples were either wet-ground or possessed a Fe_3C rich or $FeCO_3$ rich layer on the steel surface.

Figure 11: Hydrogen permeation curves performed on API 5L X65 samples in CO_2-saturated 3.5 wt.% NaCl solution at room temperature and pH 3.8. Samples were either wet-ground or possessed a Fe_3C rich or $FeCO_3$ rich layer on the steel surface.

Figure 12: Hydrogen permeation test curves performed on API 5L X65 samples in CO_2-saturated 3.5 wt.% NaCl solution at room temperature and pH 3.8. Wet-ground surface samples were exposed for 180h and the Fe_3C enrichment on the steel surface occurred during the test.

Figure 13: Potentiometry curves performed on API 5L X65 samples in CO_2-saturated 3.5 wt.% NaCl solution at room temperature and pH 3.8. Samples were wet-ground surface were exposed for 180h. There was Fe_3C enrichment on the steel surface during the test.

Figure 14: Stress versus time curves of an API 5L X65 steel in CO_2-saturated 3.5 wt. % NaCl solution under the strain rate $4.7x10^{-6}$ s^{-1}.

Figure 15: SEM: Fracture surfaces and measured diameters of the API 5LX65 steel after SSRTs in air and in CO_2-saturated environment. (a) and (b) Air. (c) and (d) Fe_3C rich surface, in CO_2-saturated environment condition B2. (e) and (f) $FeCO_3$ filmed surface, in CO_2-saturated environment condition C2. Magnification: 50x.

Figure 16: SEM: Lateral surfaces of the carbon steel after SSRTs in air and in CO_2-saturated environment. (a) Air. (b) Fe_3C rich surface, condition B2. (c) $FeCO_3$ filmed surface, condition C2. Magnification: 100x.

Figure 17: SEM: Fracture surfaces of the carbon steel after test in air and in B2 and C2 conditions, respectively. Air: (a) Center; (b) Edge. Fe_3C rich surface, condition B2: (c) Center; (d) Edge. $FeCO_3$ filmed surface, condition C2: (e) Center; (f) Edge. Magnification: 500x.

Tables

Table 1: Elemental composition (wt.%) of API 5L X65 carbon steel

Table 2: Corrosion potentials in CO_2-saturated 3.5 wt.% NaCl solution in pH 3.8 for the different surface conditions, equilibrium potential for H^+/H_2 reduction reaction and H^+/H_2 driving force .

Table 3: Parameters obtained from a triplicate of data hydrogen permeation curves, according to ASTM G148 [18].

Table 4: Statistical analysis of the steady state hydrogen flow, effective hydrogen diffusivity, permeability and surface hydrogen concentration on cathodic side of sample.

Table 5: Parameters obtained from 180h hydrogen permeation tests, according to ASTM G148 [18] and statistical analysis of the steady state hydrogen flow, effective hydrogen diffusivity, permeability and surface hydrogen concentration on cathodic side of sample.

Table 6: Statistical analysis of reduction in area (RA) and time-to-failure (TTF).

Table 7: Ratio of reduction in area (RRA) and ratio of time-to-failure (RTTF) of the API 5L X65 steel.